

# Modeling the refractive index profile $n(z)$ of polar ice for ultra-high energy neutrino experiments

S. Ali,<sup>1</sup> P. Allison,<sup>2</sup> S. Archambault,<sup>3</sup> J.J. Beatty,<sup>2</sup> D.Z. Besson,<sup>1</sup> A. Bishop,<sup>4</sup> P. Chen,<sup>5</sup> Y.C. Chen,<sup>5</sup> B.A. Clark,<sup>6</sup> W. Clay,<sup>7</sup> A. Connolly,<sup>2</sup> K. Couberly,<sup>1</sup> L. Cremonesi,<sup>8</sup> A. Cummings,<sup>9,10,11</sup> P. Dasgupta,<sup>2</sup> R. Debolt,<sup>2</sup> S. de Kockere,<sup>12</sup> K.D. de Vries,<sup>12</sup> C. Deaconu,<sup>7</sup> M. A. DuVernois,<sup>4</sup> J. Flaherty,<sup>2</sup> E. Friedman,<sup>6</sup> R. Gaior,<sup>3</sup> P. Giri,<sup>13</sup> J. Hanson,<sup>14</sup> N. Harty,<sup>15</sup> K.D. Hoffman,<sup>6</sup> J.J. Huang,<sup>5</sup> M.-H. Huang,<sup>5,16</sup> K. Hughes,<sup>2</sup> A. Ishihara,<sup>3</sup> A. Karle,<sup>4</sup> J.L. Kelley,<sup>4</sup> K.-C. Kim,<sup>6</sup> M.-C. Kim,<sup>3</sup> I. Kravchenko,<sup>13</sup> R. Krebs,<sup>9,10</sup> C.Y. Kuo,<sup>5</sup> K. Kurusu,<sup>3</sup> U.A. Latif,<sup>12</sup> C.H. Liu,<sup>13</sup> T.C. Liu,<sup>5,17</sup> W. Luszczyk,<sup>2</sup> K. Mase,<sup>3</sup> M.S. Muzio,<sup>9,10,11</sup> J. Nam,<sup>5</sup> R.J. Nichol,<sup>8</sup> A. Novikov,<sup>15</sup> A. Nozdrina,<sup>1</sup> E. Oberla,<sup>7</sup> Y. Pan,<sup>15</sup> C. Pfendner,<sup>18</sup> N. Punsuebsay,<sup>15</sup> J. Roth,<sup>15</sup> A. Salcedo-Gomez,<sup>2</sup> D. Seckel,<sup>15</sup> M.F.H. Seikh,<sup>1</sup> Y.-S. Shiao,<sup>5,19</sup> D. Smith,<sup>7</sup> S. Toscano,<sup>20</sup> J. Torres,<sup>2</sup> J. Touart,<sup>6</sup> N. van Eijndhoven,<sup>12</sup> A. Vieregge,<sup>7</sup> M.-Z. Wang,<sup>5</sup> S.-H. Wang,<sup>5</sup> S.A. Wissel,<sup>9,10,11</sup> C. Xie,<sup>8</sup> S. Yoshida,<sup>3</sup> and R. Young<sup>1</sup>

(ARA Collaboration)

<sup>1</sup>*Dept. of Physics and Astronomy, University of Kansas, Lawrence, KS 66045*

<sup>2</sup>*Dept. of Physics, Center for Cosmology and AstroParticle Physics, The Ohio State University, Columbus, OH 43210*

<sup>3</sup>*Dept. of Physics, Chiba University, Chiba, Japan*

<sup>4</sup>*Dept. of Physics, University of Wisconsin-Madison, Madison, WI 53706*

<sup>5</sup>*Dept. of Physics, Grad. Inst. of Astrophys., Leung Center for Cosmology and Particle Astrophysics, National Taiwan University, Taipei, Taiwan*

<sup>6</sup>*Dept. of Physics, University of Maryland, College Park, MD 20742*

<sup>7</sup>*Dept. of Physics, Enrico Fermi Institute, Kavli Institute for Cosmological Physics, University of Chicago, Chicago, IL 60637*

<sup>8</sup>*Dept. of Physics and Astronomy, University College London, London, United Kingdom*

<sup>9</sup>*Center for Multi-Messenger Astrophysics, Institute for Gravitation and the Cosmos, Pennsylvania State University, University Park, PA 16802*

<sup>10</sup>*Dept. of Physics, Pennsylvania State University, University Park, PA 16802*

<sup>11</sup>*Dept. of Astronomy and Astrophysics, Pennsylvania State University, University Park, PA 16802*

<sup>12</sup>*Vrije Universiteit Brussel, Brussels, Belgium*

<sup>13</sup>*Dept. of Physics and Astronomy, University of Nebraska, Lincoln, Nebraska 68588*

<sup>14</sup>*Dept. Physics and Astronomy, Whittier College, Whittier, CA 90602*

<sup>15</sup>*Dept. of Physics, University of Delaware, Newark, DE 19716*

<sup>16</sup>*Dept. of Energy Engineering, National United University, Miaoli, Taiwan*

<sup>17</sup>*Dept. of Applied Physics, National Pingtung University, Pingtung City, Pingtung County 900393, Taiwan*

<sup>18</sup>*Dept. of Physics and Astronomy, Denison University, Granville, Ohio 43023*

<sup>19</sup>*National Nano Device Laboratories, Hsinchu 300, Taiwan*

<sup>20</sup>*Universite Libre de Bruxelles, Science Faculty CP230, B-1050 Brussels, Belgium*

(Dated: June 12, 2024)

We develop an *in-situ* index of refraction profile using the transit time of radio signals broadcast from an englacial transmitter to 2-5 km distant radio-frequency receivers, deployed at depths up to 200 m. Maxwell's equations generally admit two ray propagation solutions from a given transmitter, corresponding to a direct path (D) and a refracted path (R); the measured D vs. R (dt(D,R)) timing differences provide constraints on the index of refraction profile near South Pole, where the Askaryan Radio Array (ARA) neutrino observatory is located. We constrain the refractive index profile by simulating D and R ray paths via ray tracing and comparing those to measured dt(D,R) signals. Using previous ice density data as a proxy for  $n(z)$ , we demonstrate that our data strongly favors a glaciologically-motivated three-phase densification model rather than a single exponential scale height model. Simulations show that the single exponential model overestimates ARA neutrino sensitivity compared to the three-phase model.

## I. INTRODUCTION

Ultra-High Energy Neutrino (UHEN) experiments such as the Radio Neutrino Observatory in Greenland (RNO-G), the Askaryan Radio Array (ARA), and the IceCube experiment seek to extend the energy window of observed neutrinos from MeV, typical of solar to  $>$ PeV ('cosmogenic') energy scales [1],[2],[3]. Radio provides a cost-effective method for constructing detectors with a large detection volume, as radio signals propagate far-

ther in ice compared to optical signals. A major motivation of UHEN experiments is to complement observations of ultra-high energy charged cosmic rays (UHECR) from distant astronomical sources. UHEN are emitted following collisions of UHECR with matter or the Cosmic Microwave Background. Due to their lack of charge and small cross-section, neutrinos are able to propagate through obstacles that would be otherwise opaque to cosmic rays. However, these same weakly interacting characteristics render detection difficult.

Radio propagation in ice, over kilometer-long distance scales, is a salient feature of radio neutrino experiments. Since, as the neutrino energy increases, the expected neutrino flux decreases, radio neutrino experiments seek to detect high energy cosmic neutrinos by scanning a large volume over a long exposure time, thereby compensating for the sharp drop in flux with neutrino energy.

Simulations which incorporate models of the complex-valued ice permittivity are used to estimate the sensitivity of UHEN experiments. The real part of the complex permittivity dictates the ray path followed from interaction point to receiver, while the imaginary part quantifies the degree to which signal is absorbed in-ice. Given the non-magnetic nature of ice, its permittivity relates directly to the refractive index profile through  $n = \sqrt{\epsilon_r}$  where  $\epsilon_r$  is the real part of the ice permittivity. UHEN experiments assume a depth-dependent refractive index. For a given receiver, the varying index of refractive profile in the upper 150m generates, by Fermat's Least Time Principle, curved rather than rectilinear ray trajectories, resulting in a 'shadowed' neutrino interaction volume inaccessible to that receiver at large horizontal displacements. At the lowest detectable neutrino energies, where the flux is highest, the extent of the shadowed zone is the primary determinant of the neutrino interaction volume visible to a given receiver, and therefore the number of detected neutrinos.

Current simulation and calibration efforts in ARA and RNO-G assume a refractive index profile that follows a single exponential dependence on depth, as expected for a self-gravitating fluid. Glaciological studies of ice density as a function of depth, however, suggest that densification occurs in multiple stages. Although some 2-stage models have been prescribed for the first 100m[4, 5], ARA station antennas deeper than 100m necessitate use of an extended, 3-stage model. Using timing data from a pulser lowered into the ice, we can test a piecewise function separated into these 3 stages against a simpler one-stage or two-stage exponential model.

## II. ICE DENSIFICATION AND THE REFRACTIVE INDEX

Our model assumes a linear dependence of refractive index on density. According to Sorge's Law [6], density is constant over time at a certain depth given constant snow accumulation and constant temperature. (In reality, the snow accumulation and temperature conditions are not constant which leads to density fluctuations; in what follows, we neglect such effects, as well as the possible effect of impurities, as second-order perturbations.) In our model, the densification rate of snow is taken to be proportional to the change in pressure due to the weight of the snow overburden, leading to the exponential form

$$\rho(z) = \rho_f - b_0 e^{Cz} \quad (1)$$

where  $\rho_f$  is the density of deep ice,  $\rho_f - b_0$  is the density of snow at the surface, and  $C$  is a proportionality constant describing the densification rate. This model is later converted to  $n(z)$ .

Theoretical and empirical models of ice density as a function of depth suggest two boundaries that affect the ice densification rate as the ice density crosses certain thresholds[7, 8]. We note that the density profile for ice near Summit Station, Greenland, where the RNO-G experiment is located, differs from the South Pole, where the ARA experiment is located, so these transition depths correspondingly differ. The first boundary at 550 kg/m<sup>3</sup> separates the snow and firn regions. This boundary occurs around 15m and 20m of depth for Summit and South Polar ice, respectively, and is the better-studied of the two boundaries [4],[5]. The second boundary, between 820-840 kg/m<sup>3</sup>, separates the firn and bubbly ice regions. This boundary occurs around depths of 80m vs. 100m for Summit vs. South Polar ice, respectively. The ice is considered to be fully formed in the third region, but there still exist air pockets within the ice that reduce the overall density relative to  $\rho_f$ . These air pockets are crushed under greater pressure as depth increases, asymptotically reaching the  $\rho_f \sim 920$  kg/m<sup>3</sup> density of typical deep ice (pure ice at -30° C). Figure 1 shows ice density data taken from various sources in Greenland as a function of depth.

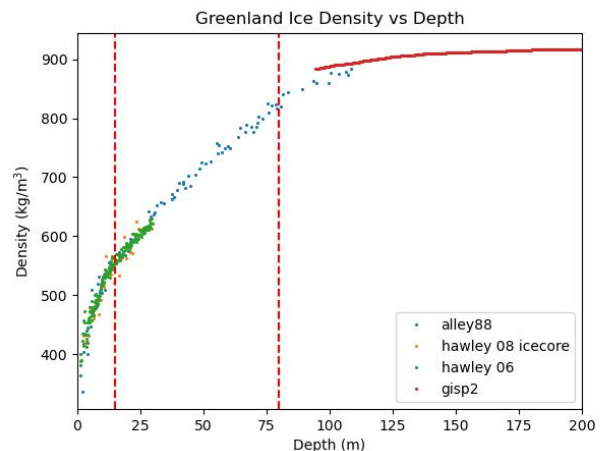


FIG. 1. Greenland ice density as function of depth. Red dotted lines (14.9m, 80m) separate snow, firn, and bubbly ice regions. Greenland ice density data have been taken from [9],[10],[11],[12].

Ice density is converted to index of refraction  $n(z)$  using a linear relationship based on a study of dielectric constant vs specific gravity in the McMurdo ice shelf located along the coast of Antarctica [13]:

$$n(z) = 1 + A\rho, \quad (2)$$

where  $\rho$  is the ice specific-gravity and  $A$  is a proportionality constant, which can be estimated from the con-

straint that deep, bulk ice has a refractive index corresponding to the measured value of  $1.778 \pm 0.006$  [14]. Different fits to data sets in the McMurdo ice shelf give a range of possible  $A$  values from 0.840-0.858. Application of equation (2) translates density data into  $n(z)$  data, to which we have customarily fit exponentials of the form:

$$n(z) = 1.78 - e^{cz}. \quad (3)$$

Figure 2 shows single exponential fits as well as 3-stage piecewise exponential fits for which the 3-stage model uses equation (3) to solve for the transition points separating the three densification regions. (Since there are fewer measurements in the bubbly ice region, the third exponential parameter of the SPICE based model (5) described below is constrained by SPICE  $dt(D,R)$  data, as outlined in Section VI instead of density data.)

The density data are converted to refractive index using equation (2) with a constant  $A = 0.845$ . Using this constant gives an asymptotic  $n(z)$  value of approximately 1.78 for the  $920 \text{ kg/cm}^3$  asymptotic density seen in deep Antarctic ice [8]. This value is consistent with a very recent (2023) precision determination of the deep ice refractive index at Summit Station, Greenland obtained by correlating radar echoes with internal layers observed in ice cores [16].

Fitting an exponential function to the ice density vs. depth relation is appealing due to the expected dependence of gravitational pressure with depth. However, these data suggest that an exponential fit requires separate parameters for each of the densification regions. Figure 2 illustrates how partitioning the model into 3 separate exponential functions allows for an improved fit, relative to the single exponential functions currently favored in simulations.

The South Pole Ice Core (SPICE) was drilled up to 1751m over 2014-2015 and 2015-2016 seasons with the purpose of collecting data to determine changes in atmospheric chemistry, climate, and biogeochemistry since the most recent [40 ka] glacial-interglacial cycle [17]. SPICE is useful for the purposes of this study as a borehole in proximity to the ARA stations that offers both density data and also deep pulser timing measurements. Figure 2 shows the 3 stage and single exponential models based on converted density data from Greenland and SPICE. In the case of SPICE fits, we compare a single exponential

$$n(z) = 1.78 - 0.45e^{-0.0132z} \quad (4)$$

to the 3 stage model parameterization:

$$z < 20.5\text{m} : n(z) = 1.78 - 0.45e^{-0.0157z}$$

$$20.5\text{m} \leq z < 102\text{m} : n(z) = 1.78 - 0.32e^{-0.0113(z-20.5)}$$

$$z \geq 102\text{m} : n(z) = 1.78 - 0.13e^{-0.0335(z-102)} \quad (5)$$

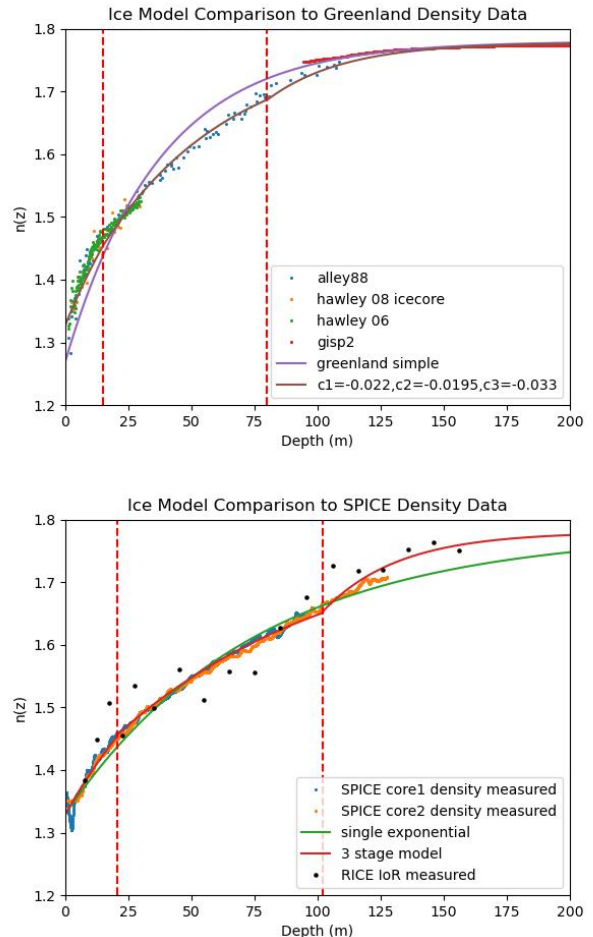


FIG. 2. Fits to indicated parameterization of density profile;  $c_1, c_2, c_3$  refer to the exponential parameters for the snow, firn, and bubbly ice regions, respectively. Equations (4) (single exponential) and (5) (3 stage model) are compared to SPICE density data [15] down to 127m depth. Deviation between the two SPICE core density measurements suggest an error of  $\pm 0.005$  in measured  $n(z)$ . 3 stage model  $c_3$  parameter constrained by SPICE  $dt(D,R)$  data (see Section VI).

taking  $z$  to be positive and increasing with depth. Equation (5) is a piecewise function with separate exponentials corresponding to the snow, firn, and bubbly ice regions, respectively. The exponentials in the firn and bubbly ice regions are shifted in depth to begin at the start of their respective regions instead of the surface; the constants  $c_1, c_2$ , and  $c_3$  refer to the constant term in the exponent for  $e^{cz}$ , in each densification regime. We now discuss verification of the revised model (Equations (4) and (5)) using ARA deep pulser data.

### III. DEEP PULSER DATA

A typical ARA station is shown in Figure 3. Each station consists of 4 vertical strings of radio receiver anten-

nas buried in 4 different holes with an inter-string lateral separation of order 20 meters. Each string consists of 2 horizontally polarized (Hpol) and 2 vertically polarized (Vpol) antennas. This allows the stations to record both Hpol and Vpol signals, as well as infer the polarization of a signal based on the relative amplitudes of the signals registered on the Hpol vs. Vpol antennas. The array of antennas also allows for the reconstruction of a source location based on the relative timings for signals received by multiple antennas. For a typical station, the top Hpol to bottom Vpol antennas are deployed at depths ranging from 170-200m. Nearby englacial pulsers are used to calibrate channel positions using relative timing differences as well as calibrate source reconstruction precision and accuracy. An accurate  $n(z)$  model is essential to obtain an accurate calibration.

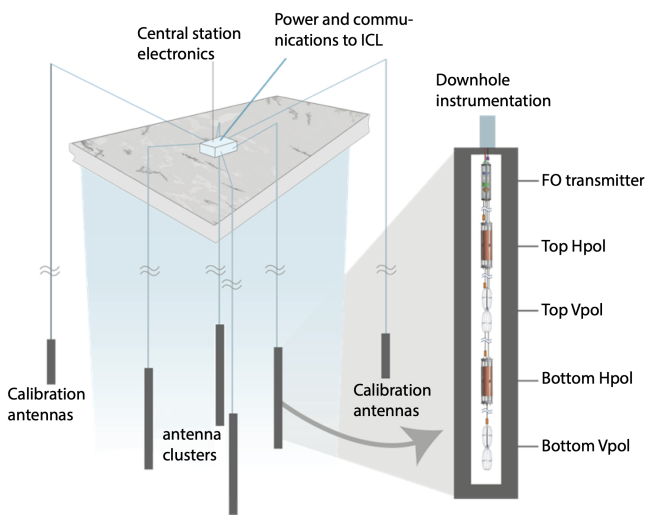


FIG. 3. Typical ARA station layout. There are a total of 16 antennas (8 Hpol and 8 Vpol) ranging from 170-200m in depth.

For electromagnetic waves traveling through a medium with variable refractive index, Maxwell’s equations, in general, admit two ray propagation solutions from a given source point to a given receiver point. Observationally, this corresponds to a ‘double pulse’ waveform. The first arriving signal is designated as the direct (D) ray path while the second arriving signal is designated the reflected or refracted (R) ray path. By measuring the arrival time of the leading edge of each of the two signals, we can calculate the timing difference  $dt(D,R)$ .

The  $dt(D,R)$  timing difference offers powerful calibration constraints for a few reasons. One concern in timing signals to the station antennas is uncertainties in the time required for signal to travel from an antenna deep in the ice to the data collection software, referred to as cable delay.  $dt(D,R)$  is immune to cable delay uncertainties since the cable delays are equal for the D and R signals on a single channel. The  $dt(D,R)$  method is also particularly useful for testing  $n(z)$  models due to the dif-

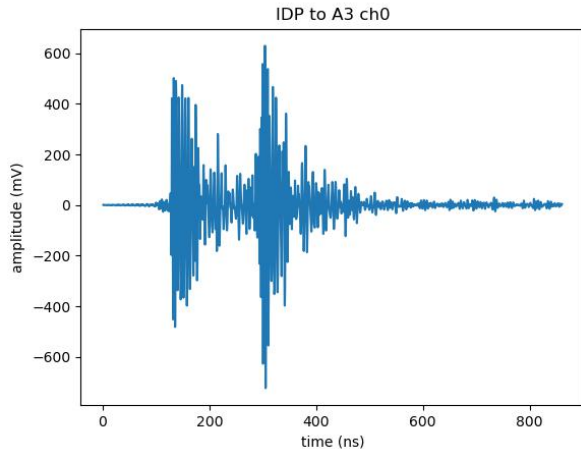


FIG. 4. Example stationary IceCube deep pulser (IDP) averaged waveform at 1400m depth showing the direct (first) and refracted (second) signals measured in ARA station A3.

ferences between the D and R optical paths (see Figure 5). The R ray path travels through ice well above the receiver antenna which allows for testing a greater range of depths for  $n(z)$ . This compares favorably in testing  $n(z)$  to the timing method of relative timing differences between channels measured using the nearby calibration pulsers which only tests  $n(z)$  over the limited depth range of the deployed ARA antennas. From a science perspective, since  $dt(D,R)$  depends on the range to source location, it can also be used as a powerful constraint in neutrino reconstruction, independent of conventional interferometric techniques.

Figure 4 shows an example ARA averaged waveform from a stationary deep pulser deployed in one of the ice-holes drilled for the IceCube experiment (referred to as IDP;  $z=1400$  m). The averaging results in a reduction of incoherent noise before the pulse as well as some variation just before the pulse arrives, likely due to slight variations in arrival time between events, and/or misalignment of single waveforms in our averaging procedure. The deep pulser is horizontally displaced by typical distances of 1-5 km, depending on the ARA receiver station. This IDP source signal was observed in all 5 ARA stations. Data from a moving deep pulser lowered into the SPICE borehole in the 2018-2019 seasons (referred to as SDP) is also useful in discriminating between refractive index models. A transmitter (South Pole UNiversity of Kansas Pressure Vessel Antenna, or SPUNK PVA) source was lowered into the SPICE borehole located 2-4km from stations A2-A5 [15]. This deep pulser source emitted 1 pulse per second (pps) signals as it was lowered into the hole down to a depth of approximately 1700m. Stations began receiving double pulse signals once the transmitter emerged from the shadow zone (around a depth of 500–700m, depending on the receiver station) resulting in a dataset of  $dt(D,R)$  pulses recorded to  $z=1300$ m. Since the D and

R ray paths differ over this range, this dataset provides a check on the consistency of  $n(z)$  models.[18]

#### IV. SIMULATED DEEP PULSER SIGNALS

Ray paths, either IDP or SDP, are simulated using the numerical ray tracer `RadioPropa` [19]. Simulated ray paths give 2 possible solutions (D and R) depending on the source and receiver positions for a given  $n(z)$  model. The travel time is calculated for each of the ray paths, and  $dt(D,R)$  is calculated directly from the difference in travel time for the two paths. Figure 5 shows the simulated ray paths from a 1300m deep source to an ARA antenna.

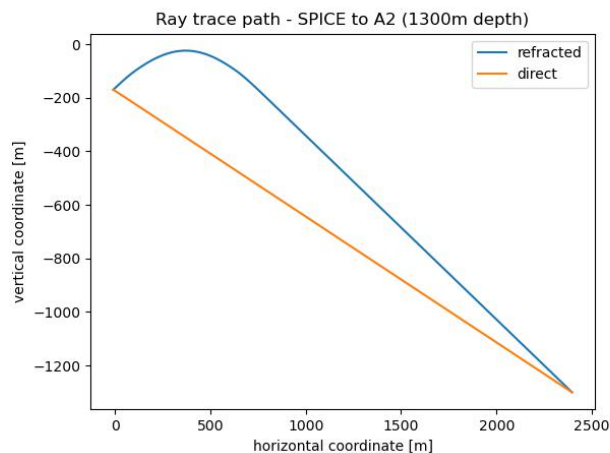


FIG. 5. Example simulated direct and refracted ray paths from a 1300m deep pulse from SPICE borehole to ch 0 of ARA station 2.

DP waveforms can also be simulated using `NuRadioMC`, a Monte Carlo simulation software suite that can be used to simulate signal waveforms and determine the neutrino detection volume of radio neutrino detectors [20]. `NuRadioMC` simulations are currently based on equation (4). (Full implementation of the 3 stage model into these simulations is currently in progress.) In addition to relative signal arrival times, simulated waveforms can be compared to the measured waveforms in terms of the relative amplitudes of the D and R signals as well as frequency content; in what follows we consider only timing information.

#### V. SNOW ACCUMULATION IMPACT ON REFRACTIVE INDEX PROFILE

Before comparing our simulated  $dt(D,R)$  to data, it is important to consider possible effects of snow accumulation with time, since ARA receiver depths were recorded

at the time of initial deployment (2011–2013 for stations A1–A3), while SDP pulser data were recorded in December, 2018. Yearly snowfall at the South Pole increases the overall depths, relative to the surface, of antennas buried in prior years. Snow accumulation is important to consider in this analysis given the dependence of  $dt(D,R)$  on antenna depth, and the expectation that the snow overburden, for a given in-ice receiver, increases with time. A study of snow accumulation at South Pole from 1983-2010 was performed using a near-surface snow stake field near Amundsen-Scott station [21], finding an average annual snow accumulation of 274.85 mm per year with a (non statistically-significant) downward trend of  $-2.8 \pm 6.7$  mm in annual accumulation over that time period. However, the snow accumulation at the antenna depths of 170-190m should be smaller than that at the surface due to the increased density at greater depths.

ARA Station A3 was deployed during the 2012-2013 season, two years after the IceCube deep pulsers were deployed. The SPICE borehole data were taken in the 2018-2019 season, corresponding to 6 years of snow accumulation since the initial antenna depths were recorded. We calculate the snow accumulation at antenna depth by comparing  $dt(D,R)$  times from one of the two IDP transmitters to station A3, registered over a multi-year time period. Figure 6 overlays the Direct and Refracted signals for data taken over an 8 year interval. In contrast to the nearly-constant Direct signals, the Refracted signals, with much shallower trajectories, show clear discrepancies. The constancy of the Direct signals over time indicate that the variations in the observed Refracted waveforms are not the result of, e.g., hole closure effects or some other effect leading to a change in the antenna response over this timescale.

Combining data from several years and selecting those channels with the highest Signal-to-Noise Ratio, Figure 7 shows the extracted  $dt(D,R)$  times from the IC22S deep pulser to station A3 for 2015, 2018, and 2022 data. Averaged over all channels, the measured  $dt(D,R)$  from IC22S to A3 shows an increase of 6.9 ns (0.99 ns per yr) from 2015-2022 and an increase of 3.7 ns (0.93 ns per yr) from 2018-2022. Using `RadioPropa`'s numerical ray tracer we simulate the  $dt(D,R)$  times from IC22S to A3 and increase the depths of both the pulser and the station antennas to match the increased measured  $dt(D,R)$ . The measured  $dt(D,R)$  increases correspond to average snow accumulations of 1.72 m (0.25 m per yr) from 2015-2022 and 0.94 m (0.24 m per yr) from 2018-2022 using the 3 stage model (5) to simulate  $dt(D,R)$ . The 2015-2022 and 2018-2022 IC22S data imply an average annual snow accumulation (measured at  $z \sim 180$  m) of  $0.24 \pm 0.09$  m (statistical errors only). This snow accumulation rate is used to correct station antenna depths from those taken during deployment to the depths at the time of SPICE borehole data collection.

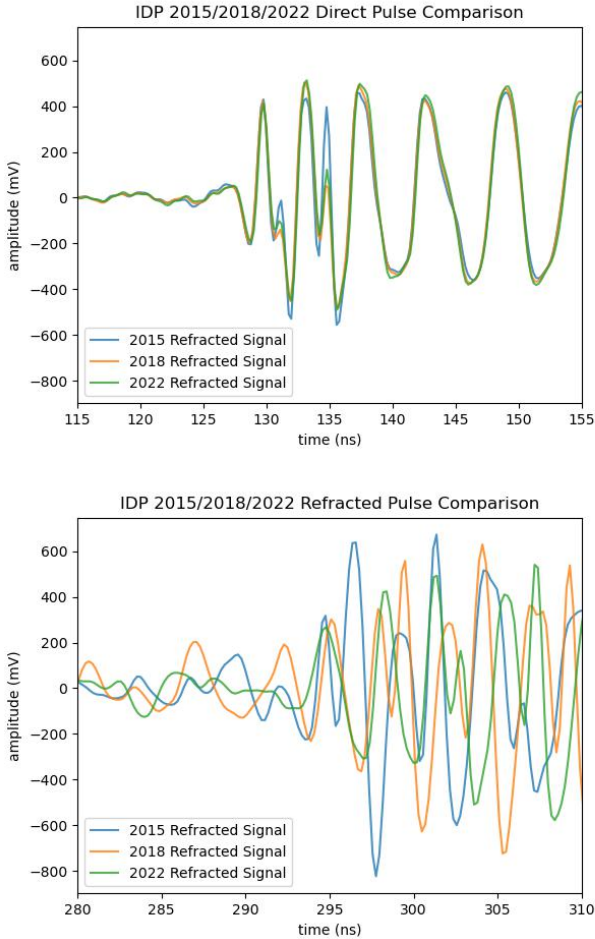


FIG. 6. Comparison of 2015 vs. 2018 vs. 2022 IceCube Deep Pulsar signals, showing Direct (top) and Refracted (bottom) signals. For the receiver channel considered (at a depth of 175 meters, and therefore close to the asymptotic ice density regime), the Direct signals are remarkably consistent with each other (indicating very little aging or hole closure effects), while the Refracted signals, which sample shallower snow and are more sensitive to refractive index changes, show evident differences.

## VI. ICE MODEL RESULTS

By lowering a pulser into the SPICE borehole,  $dt(D,R)$  data can be collected for a variety of ray paths. To ensure the transmitter is well beyond the shadow zone, we measure  $dt(D,R)$  over the depth range from 700–1300 m for most stations. Typical horizontal separations are of order 1–5 km - in the case of A3, for example, the SPICE borehole is located 3230m horizontally from that station. The measured  $dt(D,R)$  data provide constraints for the bubbly ice region. While keeping the  $c1$  and  $c2$  values fixed, based on fits to SPICE density data,  $c3$  of Equation (5) was determined via relative error minimization between measured and simulated  $dt(D,R)$  for stations A2-A4. Relative error is defined by  $\Delta dt(D,R)$  squared

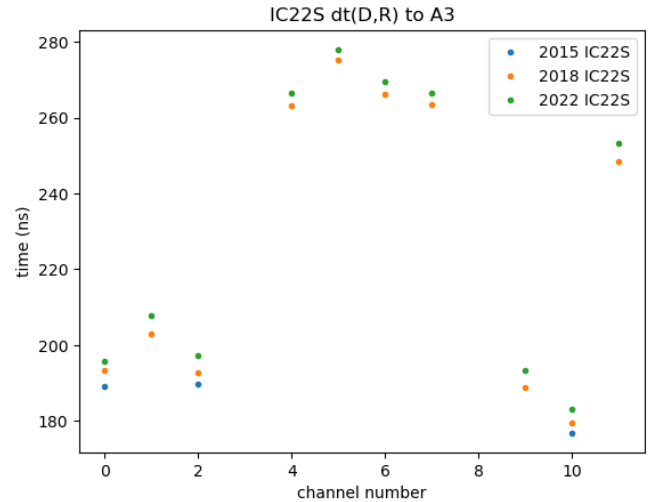


FIG. 7. Measured  $dt(D,R)$  from IC22S to A3 antennas for 3 seasons.  $dt(D,R)$  increases for later seasons in accordance with increased antenna depth due to snow accumulation. Channels 0,2,10 provide good  $dt(D,R)$  data across all 3 seasons while remaining channels include  $dt(D,R)$  data only for the 2018 and 2022 seasons.

divided by the measured  $dt(D,R)$  value for a given SPICE pulse. The total relative error is the sum across SPICE pulses to channels from stations A2-A4 at varying SPICE depths. Figure 8 shows the total relative error for  $c3$  values bracketing the minimum value.

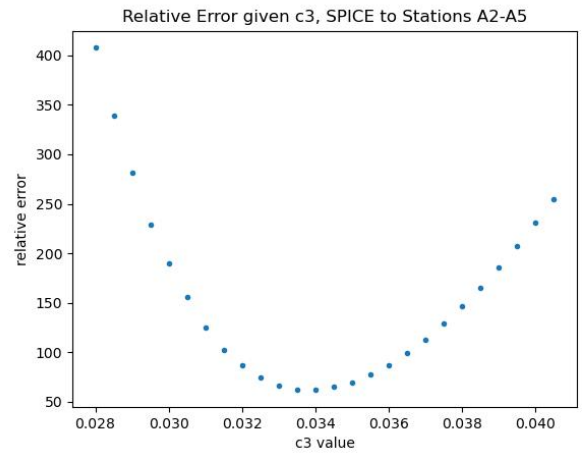


FIG. 8. Distribution of total relative error between simulated and measured  $dt(D,R)$  ( $\Delta dt(D,R)$ ) for a given  $c3$  parameter using  $c1, c2$  of Eqn. (4), summed for channels in stations A2-A4 for SPICE pulsing runs.

Figure 9 shows the measured - simulated  $dt(D,R)$  from SPICE to ARA station A3 for the  $n(z)$  models corresponding to equations (4) (single exponential) and (5) (3 stage model). ‘Measured’ times refer to  $dt(D,R)$  calculated using the arrival times of the leading edges of the

D and R signals in double pulse waveforms similar to Figure 4. Measured arrival times for the D and R signals are determined both by the crossing of an amplitude threshold as well as cross correlation of the D and R signals. The discrepancy between these methods is within 3 ns and is included in the error estimation. ‘Simulated’ times refer to calculated  $dt(D,R)$  from the D and R ray paths generated using `RadioPropa` for given source and receiver locations. Shown in Figures 9 and 10 are the differences between measured and simulated  $dt(D,R)$  for various pulsing depths (referred to as  $\Delta[dt(D,R)]$ ). The impact of uncertainties in the SDP and receiver antenna coordinates on the (D,R) time differences are assessed by varying these positions in simulations, and indicated by the  $\Delta dt(D,R)$  error bars.

As illustrated in Figure 9, the exponential model shows a trend for which measured  $dt(D,R)$  increases relative to simulated  $dt(D,R)$  at shallower depths. Even allowing for large variations in the  $b$  and  $c$  parameters, the single exponential model is still unable to resolve the trend seen in the SPICE  $dt(D,R)$  data. The discrepancy can be markedly reduced by using a 3 stage model, where the  $c3$  parameter is increased for the bubbly ice region relative to the  $c$  parameter of the single exponential. The SPICE  $dt(D,R)$  data therefore indicates that the densification rate in the bubbly ice region must be higher than what is predicted by the single exponential function.

Station A5 is located 4165m from the SPICE borehole, of order 1km further away than the other stations. This larger lateral distance also results in an increased extent of the shadowed zone, corresponding to  $dt(D,R)$  data only being measurable over a range of 850-1300m source depth. Figure 10 shows the measured - simulated  $dt(D,R)$  results, comparing the two different refractive index parameterizations (equations (4) and (5)) for station A5. The single exponential  $n(z)$  model again shows a trend as a function of SPICE depth similar to Figure 9, which is improved using the 3 stage exponential  $n(z)$  model.

Overall, stations A2 and A4 exhibit similar improvements in comparing data to simulation. Station A1, which was deployed in 2012, only to depths of 50–85 m, amidst considerable drilling and surveying challenges also shows significant improvement, albeit with significantly larger attendant systematic errors.

## VII. SHADOWED ZONE

As a source moves further away laterally from a receiver or upwards to a shallower depth,  $dt(D,R)$  decreases. Eventually, as  $dt(D,R)$  approaches 0, the D and R signals seen in Figure 4 overlap. Initially, this results in focusing that increases signal amplitude. However, beyond a certain point the bending of possible paths no longer allow signal to reach the receiver from the transmitter. An example of this might be a receiver that lies well above the refracted path shown in Figure 5 relative

to the deep pulser; as discussed previously, this region corresponds to the ‘shadowed zone’. Since refraction is determined by the  $n(z)$  model, the shadowed zone, as well as the detected neutrino rate, both depend on  $n(z)$ .

Figure 11 shows how changes in the refractive index model affect the lateral extent of the shadow zone. Depending on source depth, the three-stage model reduces the range to the shadow zone boundary by approximately 100m relative to the exponential model. Much of the difference in shadow zone between the two models results from the differing behavior in the bubbly ice region. If the  $c3$  parameter of Eqn. (5) is instead forced to match Eqn. (4), the two shadow zone boundaries are similar. The three-stage model therefore results in a more restricted accessible target volume, and correspondingly decreased neutrino sensitivity. Figure 12 compares effective volume simulations using the two ice models for a neutrino detector station with a 100m deep antenna.

## VIII. CONCLUSION

Measured  $dt(D,R)$  time differences from deep radio-frequency transmitters support a glaciologically-motivated 3 stage exponential  $n(z)$  model over a single exponential model, which tends to overestimate  $n(z)$  in the firn region. Additional density data, below 100 meters depth, would help to constrain the model further. The three-stage model also suggests a lower effective volume than predicted by the extant one-exponential  $n(z)$  model for UHEN experiments, and therefore a slightly reduced estimated neutrino detection rate. Future analysis of the amplitude and frequency content of D and R signals can help refine the  $n(z)$  model, as phenomena such as flux focusing are also sensitive to ray curvature. Comparison of simulated shadowed zone boundaries with those extrapolated from signal amplitudes as a function of depth also provides an independent check on the refractive index profile. An improved  $n(z)$  model should help provide a more accurate effective volume estimation and aid in current calibration efforts for UHEN experiments in both Greenland and the South Pole, as well as future planned experiments, such as the radio component of the IceCube-Gen2 Radio experiment.

## IX. ACKNOWLEDGMENTS

Kenny Couberly was the main author of this manuscript and led the analysis discussed. The ARA Collaboration designed, constructed, and now operates the ARA detectors. We would like to thank IceCube and specifically the winterovers for the support in operating the detector; we also express our appreciation for the authors of the `NuRadioMC` code that was used for our simulations. Data processing and calibration, Monte Carlo simulations of the detector and of theoretical mod-

els and data analyses were performed by a large number of collaboration members, who also discussed and approved the scientific results presented here. We thank the Raytheon Polar Services Corporation, Lockheed Martin, and the Antarctic Support Contractor for field support and enabling our work on the harshest continent. We are thankful to the National Science Foundation (NSF) Office of Polar Programs and Physics Division for funding support. We further thank the Taiwan National Science Councils Vanguard Program NSC 92-2628-M-002-09 and the Belgian F.R.S. FNRS Grant 4.4508.01. A. Connolly thanks the NSF for Award 1806923 and also acknowledges the Ohio Supercomputer Center. S. A. Wissel thanks the NSF for support through CAREER Award 2033500. M. S. Muzio thanks the NSF for support through MPS-Ascend Postdoctoral Award 2138121. A. Viereggs thanks the Sloan Foundation and the Research Corporation for Science Advancement, the Research Computing Center and the Kavli Institute for Cosmological Physics at the University of Chicago for the resources they provided. R. Nichol thanks the Leverhulme Trust for their support. K.D. de Vries is supported by European Research Council under the European Unions Horizon research and innovation program (grant agreement 763 No 805486). D. Besson, I. Kravchenko, and D. Seckel thank the NSF for support through the IceCube EPSCoR Initiative (Award ID 2019597)

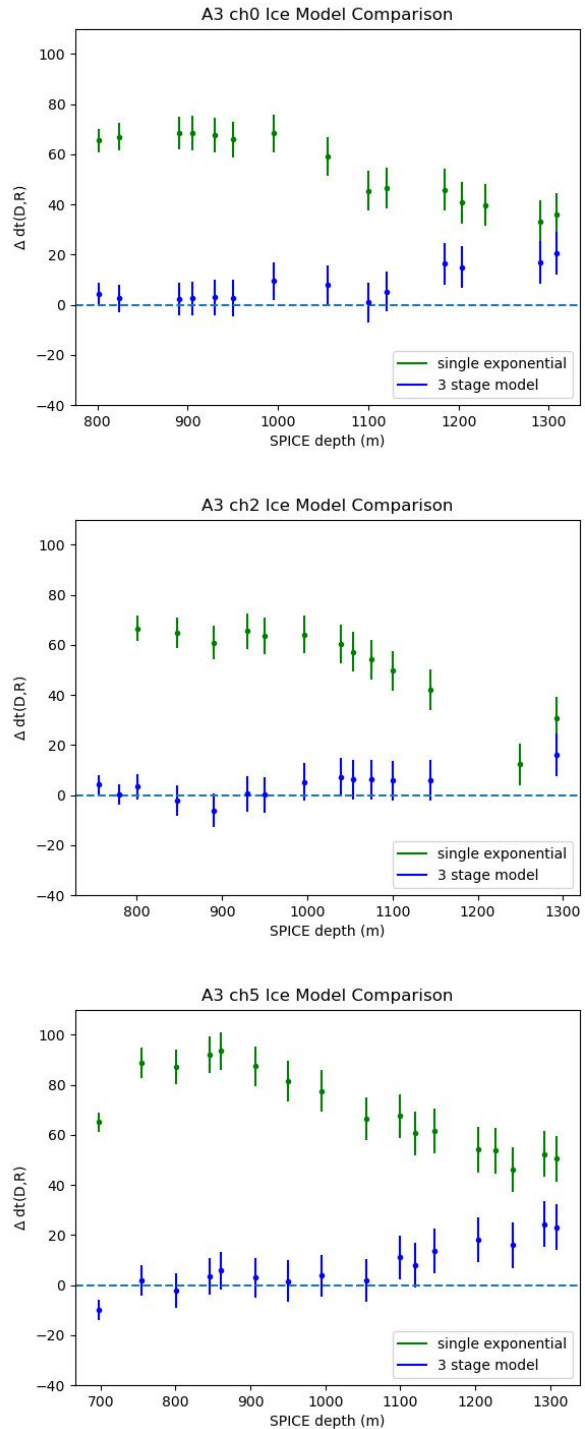


FIG. 9.  $\Delta dt(D,R)$  for signals traveling from SPICE borehole to station A3, for high SNR channels 0,2,5. Shown are comparisons of simulated vs measured  $dt(D,R)$  for both Eqn. (4) and Eqn. (5).



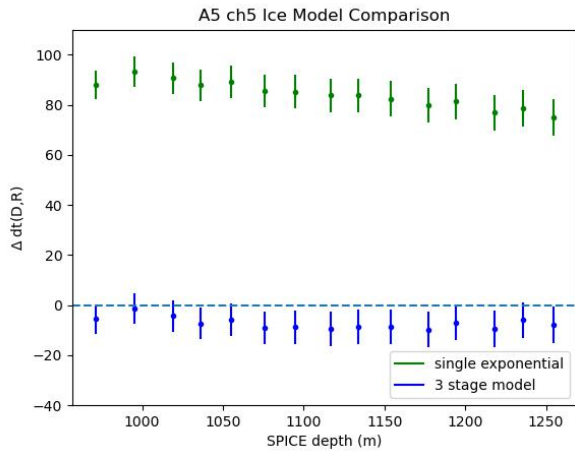
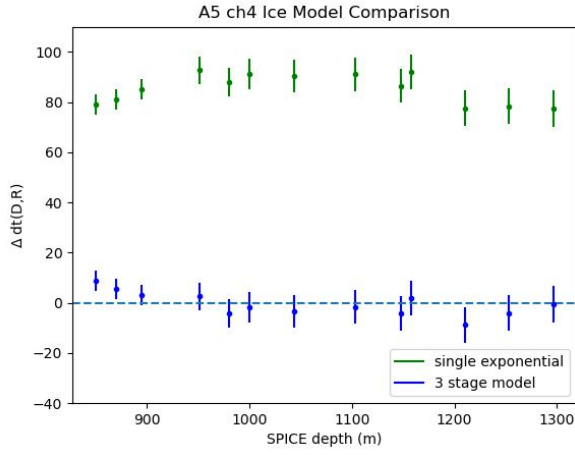


FIG. 10.  $\Delta dt(D,R)$ , extracted using Eqn. (4) and Eqn. (5) for channels 4 and 5 from station A2. The refractive index parameterization from (5) improves the trend, relative to a single exponential model, as a function of SPICE depth.

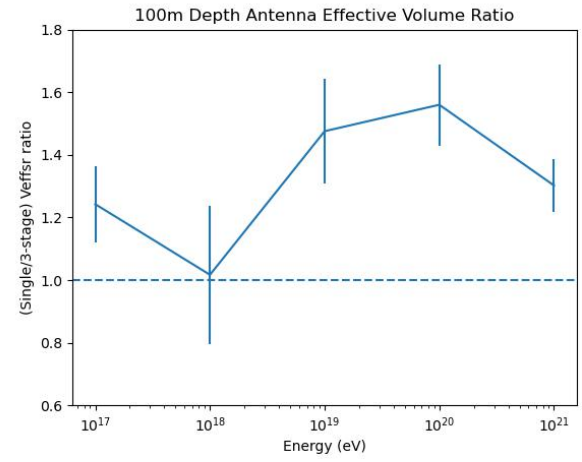
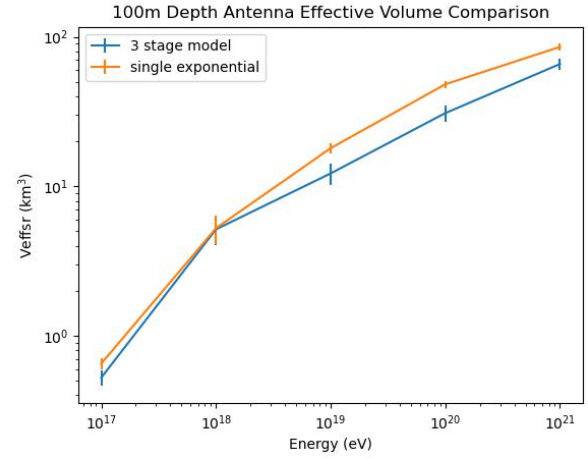


FIG. 12. Simulated effective volume (top) and ratio (bottom) plots for refractive index profiles specified by equations (4) and (5), for neutrino energies of 10<sup>17</sup>, 10<sup>18</sup>, 10<sup>19</sup>, 10<sup>20</sup>, 10<sup>21</sup> eV. Error bars shown are statistical only.

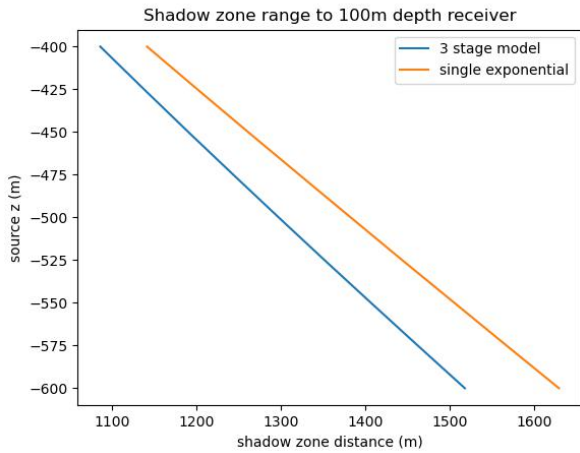


FIG. 11. Example simulated shadow zone boundary ( $r,z$ ) coordinates for a 100m depth receiver antenna, for two different refractive index models (Eqns. (4) and (5)).

- 
- [1] Juan A Aguilar, Patrick Allison, James J Beatty, Hans Bernhoff, David Zeke Besson, Nils Binglefors, Olga Botner, Sjoerd Bouma, Stijn Buitink, Katie Carter, et al. The radio neutrino observatory greenland (rno-g). In *37th International Cosmic Ray Conference (ICRC2021)*, volume 395, 2022.
- [2] Patrick Allison, R Bard, JJ Beatty, David Zeke Besson, C Bora, C-C Chen, C-H Chen, P Chen, A Christenson, A Connolly, et al. Performance of two askaryan radio array stations and first results in the search for ultrahigh energy neutrinos. *Physical Review D*, 93(8):082003, 2016.
- [3] Mark G Aartsen, R Abbasi, M Ackermann, J Adams, JA Aguilar, M Ahlers, M Ahrens, C Alispach, P Allison, NM Amin, et al. Icecube-gen2: the window to the extreme universe. *Journal of Physics G: Nuclear and Particle Physics*, 48(6):060501, 2021.
- [4] Michael M Herron and Chester C Langway. Firn densification: an empirical model. *Journal of Glaciology*, 25(93):373–385, 1980.
- [5] C Max Stevens, Vincent Verjans, Jessica Lundin, Emma C Kahle, Annika N Horlings, Brita I Horlings, and Edwin D Waddington. The community firn model (cfm) v1. 0. *Geoscientific Model Development*, 13(9):4355–4377, 2020.
- [6] Henri Bader. Sorge’s law of densification of snow on high polar glaciers. *Journal of Glaciology*, 2(15):319–323, 1954.
- [7] Andrey N Salamatin, Vladimir Ya Lipenkov, and Paul Duval. Bubbly-ice densification in ice sheets: I. theory. *Journal of Glaciology*, 43(145):387–396, 1997.
- [8] Vladimir Ya Lipenkov, Andrey N Salamatin, and Paul Duval. Bubbly-ice densification in ice sheets: II. applications. *Journal of Glaciology*, 43(145):397–407, 1997.
- [9] RB Alley, CA Shuman, DA Meese, AJ Gow, KC Taylor, KM Cuffey, JJ Fitzpatrick, PM Grootes, GA Zielinski, M Ram, et al. Visual-stratigraphic dating of the gisp2 ice core: Basis, reproducibility, and application. *Journal of Geophysical Research: Oceans*, 102(C12):26367–26381, 1997.
- [10] Richard B Alley and Bruce R Koci. Ice-core analysis at site a, greenland: preliminary results. *Annals of Glaciology*, 10:1–4, 1988.
- [11] Robert L Hawley and Elizabeth M Morris. Borehole optical stratigraphy and neutron-scattering density measurements at summit, greenland. *Journal of Glaciology*, 52(179):491–496, 2006.
- [12] Robert L Hawley, Elizabeth M Morris, and Joseph R McCONNELL. Rapid techniques for determining annual accumulation applied at summit, greenland. *Journal of Glaciology*, 54(188):839–845, 2008.
- [13] Austin Kovacs, Anthony J Gow, and Rexford M Morey. The in-situ dielectric constant of polar firn revisited. *Cold Regions Science and Technology*, 23(3):245–256, 1995.
- [14] J. A. Aguilar et al. Precision measurement of the index of refraction of deep glacial ice at radio frequencies at Summit Station, Greenland. 4 2023.
- [15] P Allison, S Archambault, JJ Beatty, DZ Besson, CC Chen, CH Chen, P Chen, A Christenson, BA Clark, W Clay, et al. Long-baseline horizontal radio-frequency transmission through polar ice. *Journal of Cosmology and Astroparticle Physics*, 2020(12):009, 2020.
- [16] Christoph Welling. Precision measurement of the index of refraction of deep glacial ice at radio frequencies at summit station, greenland. *EGUsphere*, 2023:1–14, 2023.
- [17] Kimberly Ann Casey, TJ Fudge, TA Neumann, EJ Steig, MGP Cavitte, and DD Blankenship. The 1500 m south pole ice core: recovering a 40 ka environmental record. *Annals of Glaciology*, 55(68):137–146, 2014.
- [18] Note1. A similar measurement is being planned in summer 2024 to test  $n(z)$  models in Greenland over a depth range of 300m-700m to provide double pulse signals to receiver antennas over depths from 43–100m.
- [19] Tobias Winchen. Radiopropa — a modular raytracer for in-matter radio propagation. *EPJ Web of Conferences*, 216:03002, 2019. ISSN 2100-014X. doi: 10.1051/epjconf/201921603002. URL <http://dx.doi.org/10.1051/epjconf/201921603002>.
- [20] Christian Glaser, Daniel García-Fernández, Anna Nelles, Jaime Alvarez-Muñiz, Steven W Barwick, Dave Z Besson, Brian A Clark, Amy Connolly, Cosmin Deaconu, KD de Vries, et al. Nuradiomc: Simulating the radio emission of neutrinos from interaction to detector. *The European Physical Journal C*, 80:1–35, 2020.
- [21] Matthew A Lazzara, Linda M Keller, Timothy Markle, and John Gallagher. Fifty-year amundsen-scott south pole station surface climatology. *Atmospheric Research*, 118:240–259, 2012.